

Supporting Information for

Carbon turnover times shape topsoil carbon difference between Tibetan Plateau and Arctic tundra

Donghai Wu^{1†}, Dan Liu^{2†}, Tao Wang^{2,3}, Jinzhi Ding², Yujie He⁴, Philippe Ciais⁵, Gengxin Zhang^{2*}, Shilong Piao^{1,2,3*}

¹Sino-French Institute for Earth System Science, College of Urban and environmental Sciences, Peking University, Beijing 100871, China.

²Key Laboratory of Alpine Ecology, Institute of Tibetan Plateau Research, Chinese Academy of Sciences, Beijing, 100085, China.

³CAS Center for Excellence in Tibetan Plateau Earth Sciences, Chinese Academy of Sciences, Beijing, 100085, China.

⁴Department of Earth System Science, University of California, Irvine, CA, USA.

⁵Laboratoire des Sciences du Climat et de l'Environnement, LSCE/IPSL, CEA-CNRS-UVSQ, Université Paris-Saclay, F-91191 Gif-sur-Yvette, France.

This is a list of Supplementary Materials:

Figure S1. Locations of radiocarbon soil profiles used in this study.

Figure S2. Spatial patterns of topsoil organic carbon (SOC) density in Tibetan Plateau (TP) grassland and Arctic tundra derived from three observation-based data sources.

Figure S3. Histograms of topsoil organic carbon (SOC) density in Tibetan Plateau (TP) grassland and Arctic tundra derived from three observation-based data sources.

Figure S4. Relationships between cumulative proportion of soil organic carbon (SOC) density and soil depth for Tibetan Plateau (TP) grassland and Arctic tundra.

Figure S5. Evaluation of gridded GPP products using site-level eddy flux measurements.

Figure S6. Carbon use efficiency (NPP/GPP) at a spatial resolution of 1 degree produced by combining a diagnostic ecosystem carbon balance model (DALEC2) with satellite observations and soil carbon dataset.

Figure S7. Relationship between NDVI and aboveground biomass for TP grassland.

Figure S8. Relationships between NDVI, aboveground biomass and ANPP for Arctic tundra.

Figure S9. Spatial patterns of primary production in Tibetan Plateau (TP) grassland and Arctic tundra.

Figure S10. Histograms of primary production in Tibetan Plateau (TP) grassland and Arctic tundra.

Figure S11. Spatial patterns of mean annual temperature (MAT), mean annual precipitation (MAP) and altitude in Tibetan Plateau (TP) grassland and Arctic tundra.

Figure S12. Histograms of mean annual temperature (MAT) and mean annual precipitation (MAP) using WorldClim Version 2.0 dataset in Tibetan Plateau (TP) grassland and Arctic tundra, respectively.

Figure S13. Histograms of mean annual solar radiation (MAR) and mean annual ultraviolet-B radiation (MUV-BR) in Tibetan Plateau (TP) grassland and Arctic tundra.

Figure S14. Histograms of physical soil properties from Soilgrid250m datasets in Tibetan Plateau (TP) grassland and Arctic tundra.

Figure S15. Spatial patterns of primary production in Tibetan Plateau (TP) grassland and Arctic tundra.

Figure S16. Histograms of primary production in Tibetan Plateau (TP) grassland and Arctic tundra.

Figure S17. Spatial pattern of site-based SOC turnover time in topsoil (0-10cm).

Figure S18. Distribution of SOC turnover time in topsoil (0-10cm) in the mean annual temperature (MAT) and mean annual precipitation (MAP) domain.

Figure S19. Relationships between topsoil organic carbon (SOC) turnover time and altitude.

Figure S20. Spatial patterns of topsoil organic carbon (SOC) turnover times in Tibetan Plateau (TP) grassland and Arctic tundra.

Figure S21. Uncertainties of spatial patterns of topsoil organic carbon (SOC) turnover time with 10th and 90th percentiles in Tibetan Plateau (TP) grassland and Arctic tundra.

Figure S22. Uncertainties of topsoil organic carbon (SOC) turnover time with 10th and 90th percentiles in Tibetan Plateau (TP) grassland and Arctic tundra.

Figure S23. Uncertainties of topsoil organic carbon turnover time difference between TP grassland and Arctic tundra with 10th and 90th percentiles in the climate space.

Figure S24. Ratio of carbon and nitrogen (C:N) in soil and microbes for TP grassland and Arctic tundra based on previous field investigations and meta-analyses.

Figure S25. Percentages of human appropriation of NPP in TP grassland and Arctic tundra.

Figure S1. Locations of radiocarbon (^{14}C) soil profiles used in this study. a, Tibetan Plateau (TP) grassland (21 locations). b, Arctic tundra (10 locations). The color of each symbol denotes the proportion of ^{14}C in the 0-10cm layer. The TP grassland and Arctic tundra study areas are shaded in grey.

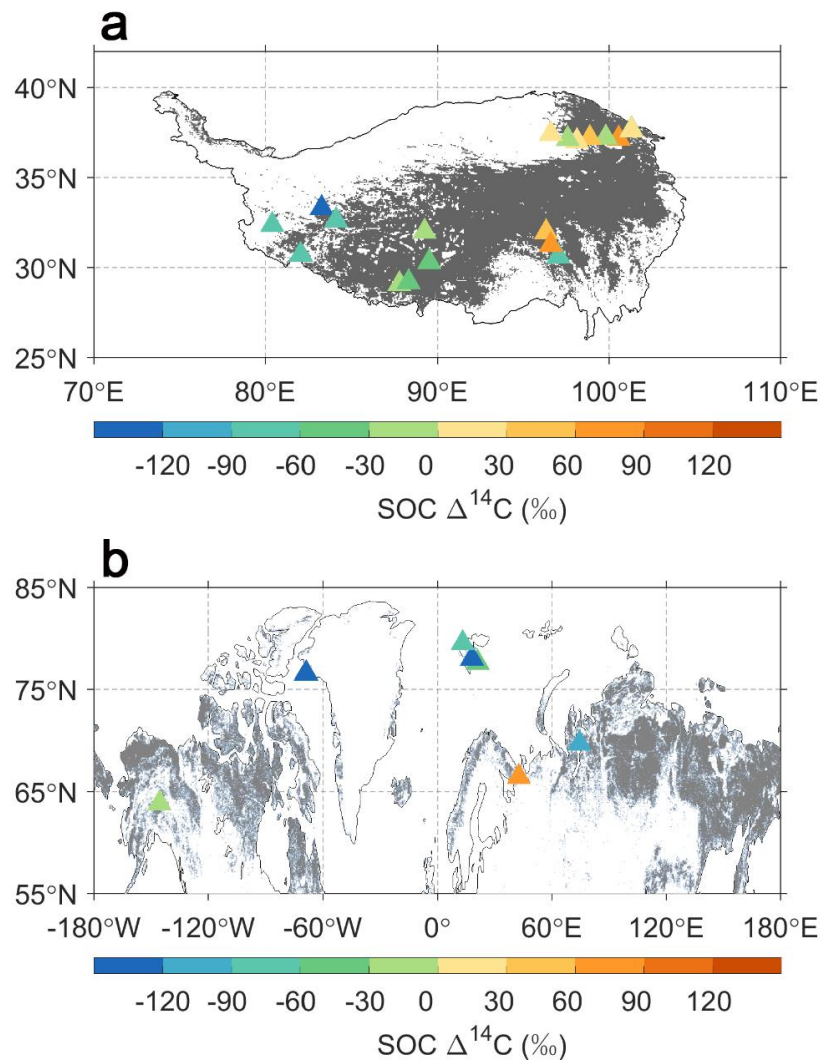


Figure S2. Spatial patterns of topsoil organic carbon (SOC) density in Tibetan Plateau (TP) grassland and Arctic tundra derived from three observation-based data sources. a-b, SoilGrids database. c-d, the World Inventory of Soil Property Estimates (WISE) dataset. e-f, Harmonized World Soil Database (HWSD) and the Northern Circumpolar Soil Carbon Database (NCSCD).

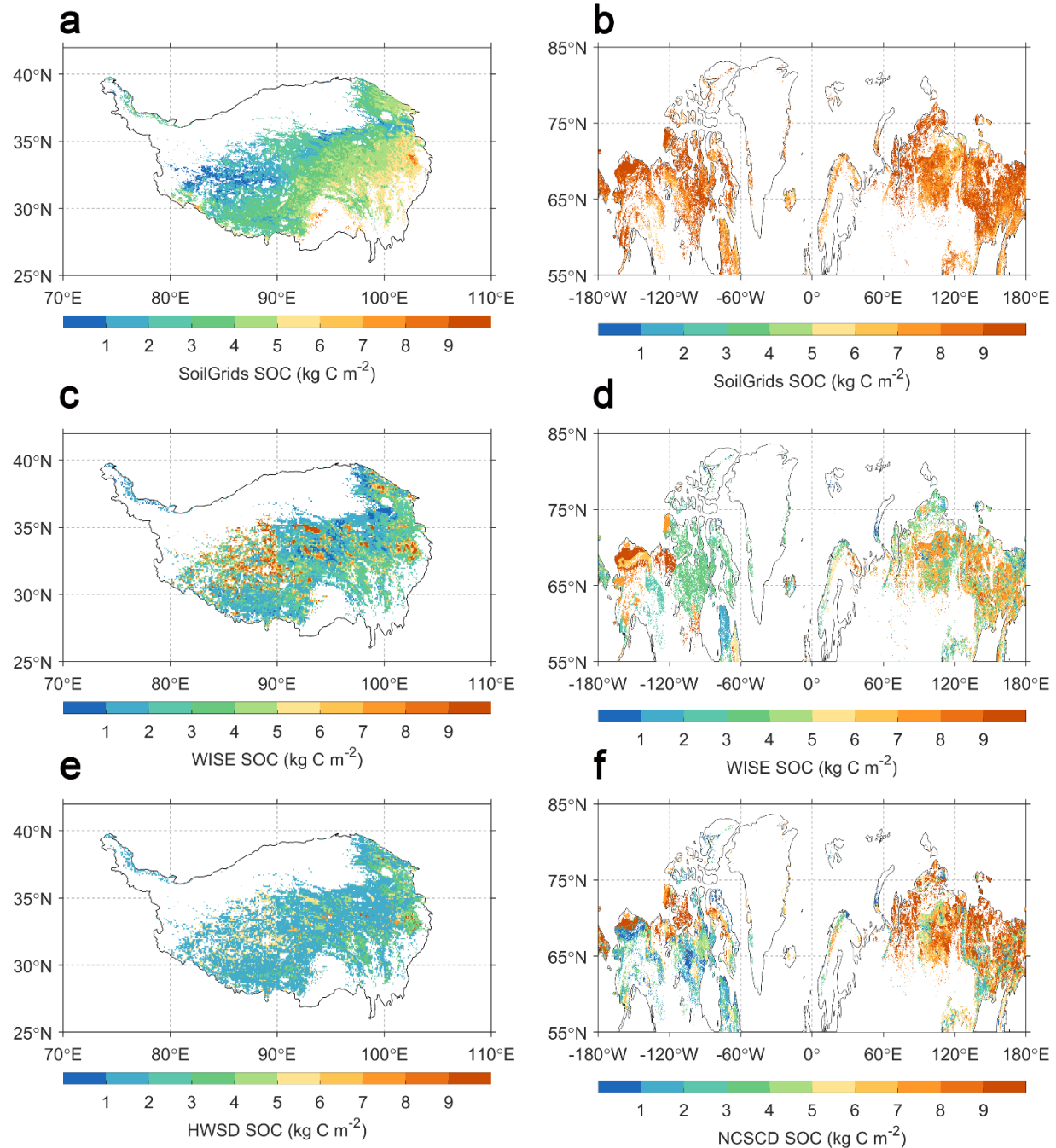


Figure S3. Histograms of topsoil organic carbon (SOC) density in Tibetan Plateau (TP) grassland and Arctic tundra derived from three observation-based data sources. a, SoilGrids database. b, World Inventory of Soil Property Estimates (WISE) dataset. c, Harmonized World Soil Database (HWSD) and the Northern Circumpolar Soil Carbon Database (NCSCD). Values in parentheses are regional-mean SOC density that is calculated by averaging gridded values over TP grassland and Arctic tundra, respectively.

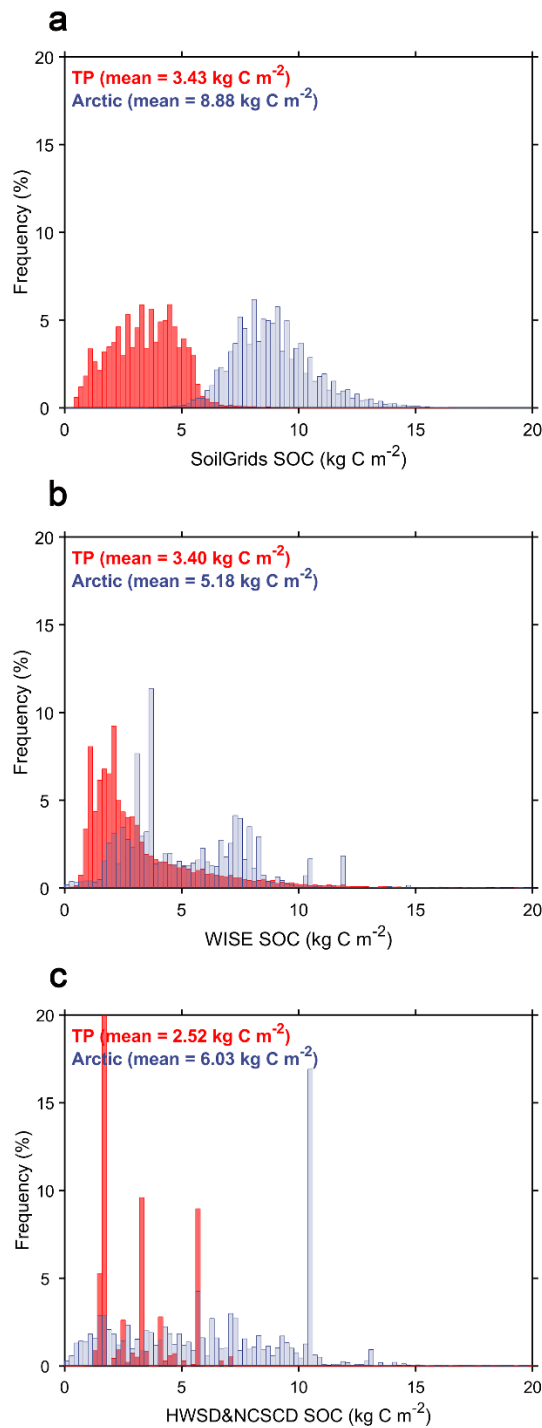


Figure S4. Relationships between cumulative proportion of soil organic carbon (SOC) density and soil depth for Tibetan Plateau (TP) grassland and Arctic tundra. The red and blue dots are based on previous field investigations and meta-analyses. The fitted functions are used for deriving SOC density in the 0-10 cm layer.

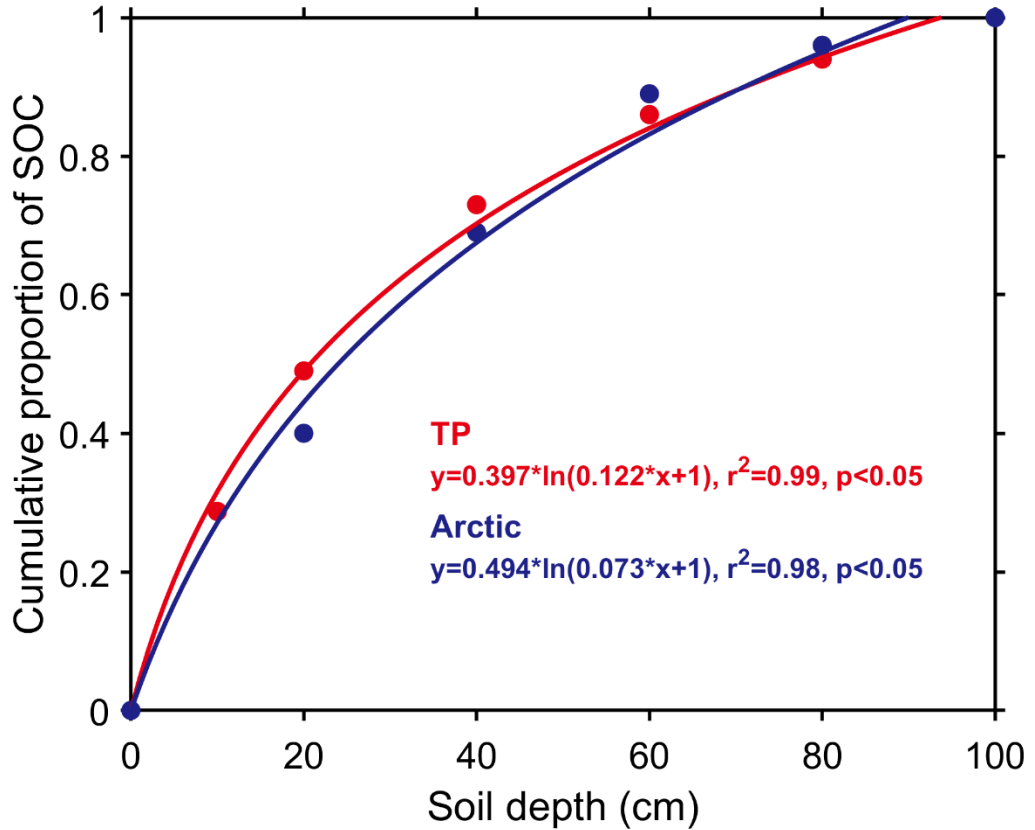


Figure S5. Evaluation of gridded GPP products using site-level eddy flux measurements. The gridded monthly GPP products are from Yao et al. (2017), Jung et al. (2011) and MODIS (MOD17A2H) for TP grassland, and from Jung et al. (2011) and MODIS for Arctic tundra. Seven sites, including Dangxiong (2004-2008), Guoluo (2007), Haibei1 (2002-2003), Haibei2 (2002-2004), Namtso (2009), Zhufeng (2009) and Arou (2008-2010), from ChinaFlux (<http://www.chinaflux.org/>) are used for evaluation in TP grassland. Four sites, including GI-Nuf (2008-2011), RU-Che (2002-2005), US-Atq (2003-2008) and US-Ivo (2004-2007), from Fluxnet2015 (<https://fluxnet.org/data/fluxnet2015-dataset/>) are used for evaluation in Arctic tundra. MODIS GPP suggested underestimation in TP grassland and overestimation in Arctic tundra. In this study, we used GPP data from Jung et al. (2011) for Arctic tundra and GPP data from Yao et al. (2017) for TP grassland, which show high quality for representing the gross photosynthesis of the two regions.

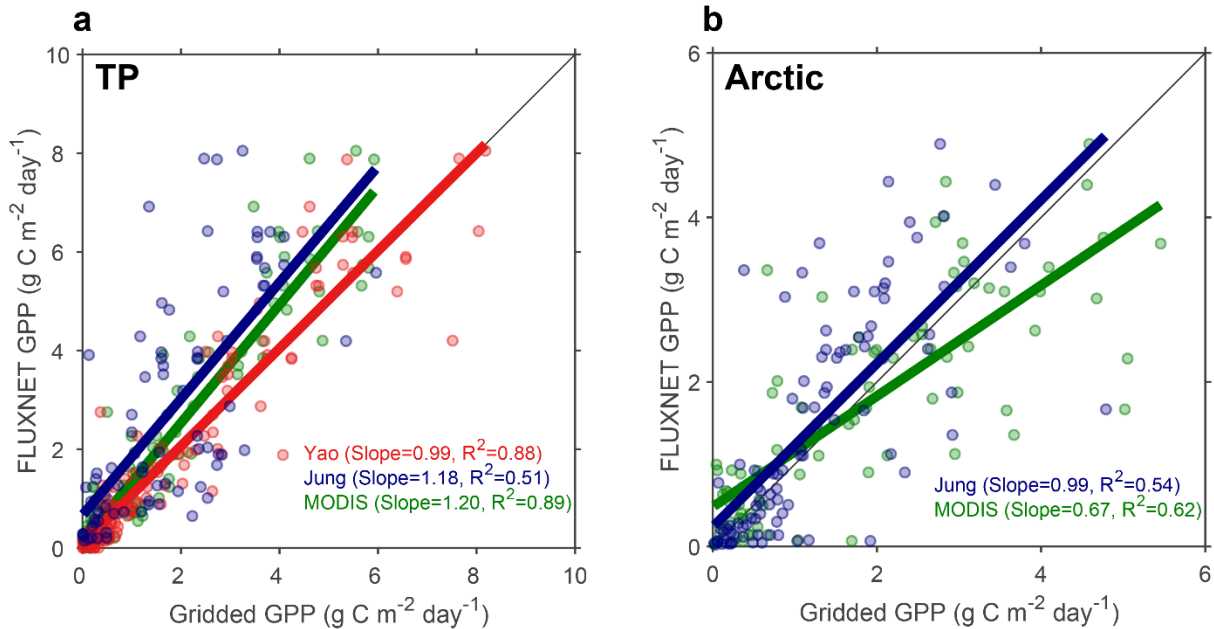


Figure S6. Carbon use efficiency (NPP/GPP) at a spatial resolution of 1 degree produced by combining a diagnostic ecosystem carbon balance model (DALEC2) with satellite observations and soil carbon dataset (Bloom et al. (2016)). a, spatial pattern of CUE in TP grassland. b, spatial pattern of CUE in Arctic tundra. c, histograms of CUE in TP grassland and Arctic tundra.

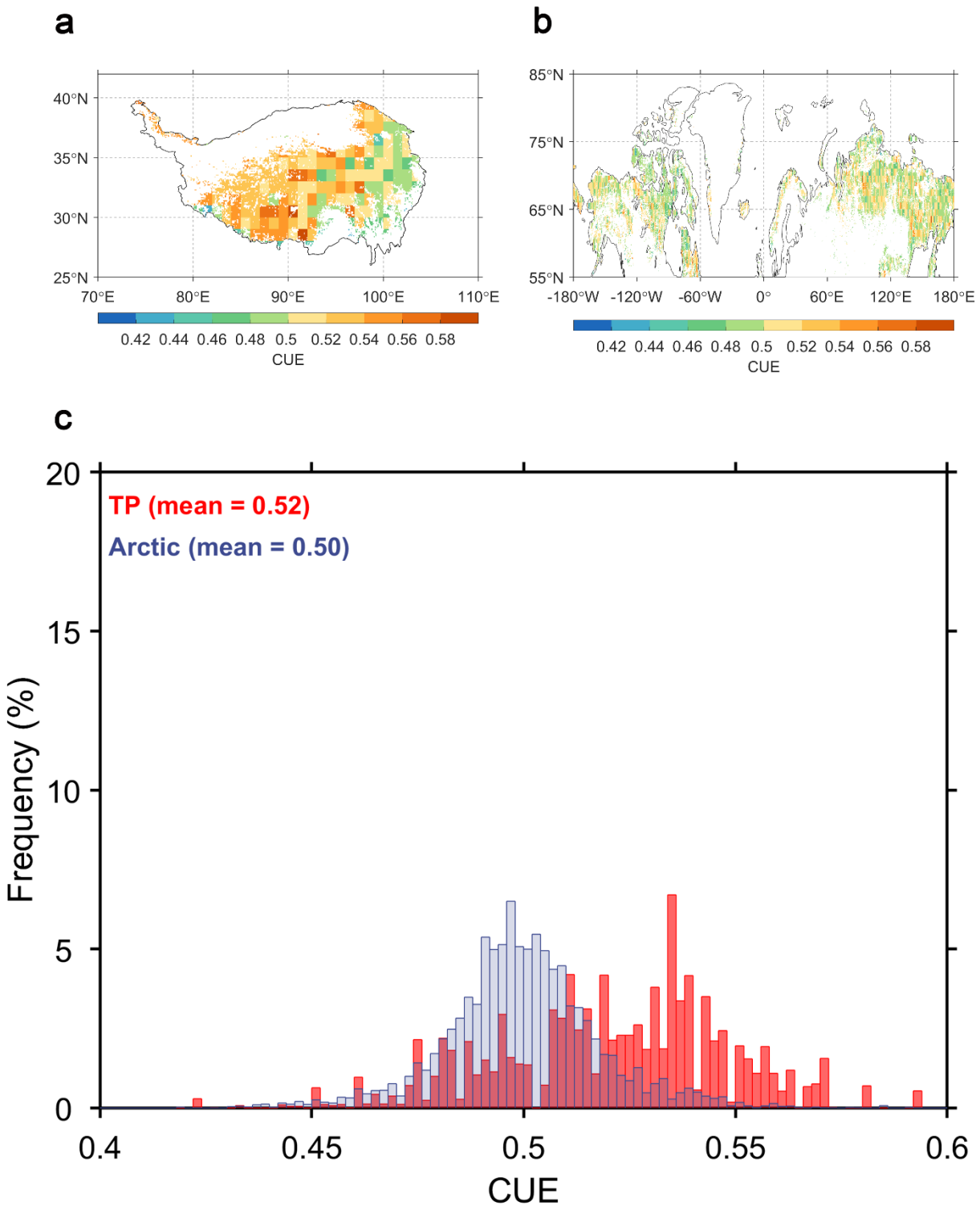


Figure S7. Relationship between NDVI and aboveground biomass for TP grassland. 115 field sites of aboveground biomass are from Yang et al. (2010). The NDVI data for each field site was extracted from a maximum annual NDVI dataset using GIMMS NDVI at a spatial resolution of 1/12 degree for the year during which the biomass was collected.

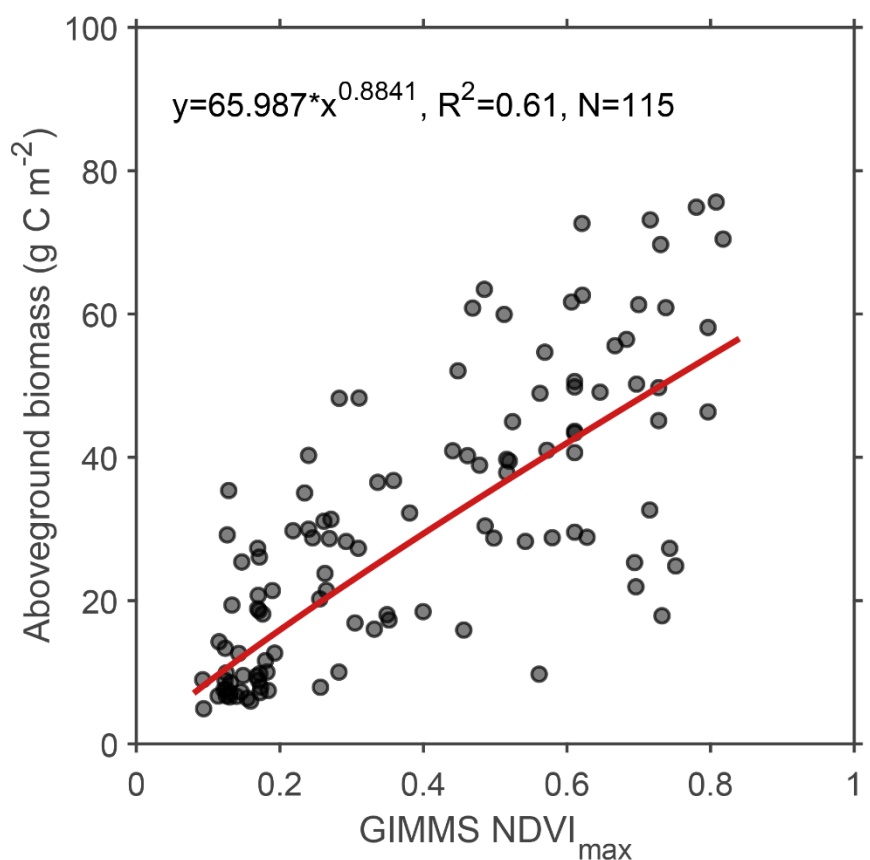


Figure S8. Relationships between NDVI, aboveground biomass and ANPP for Arctic tundra. a, relationship between NDVI and aboveground biomass. b, relationships between aboveground biomass and ANPP. 11 field sites of aboveground biomass are from Reynolds et al. (2012). 87 field sites of aboveground biomass and ANPP are from Oechel et al. (2012). The NDVI data for each field site was extracted from a maximum annual NDVI dataset using GIMMS NDVI at a spatial resolution of 1/12 degree for the year during which the biomass was collected.

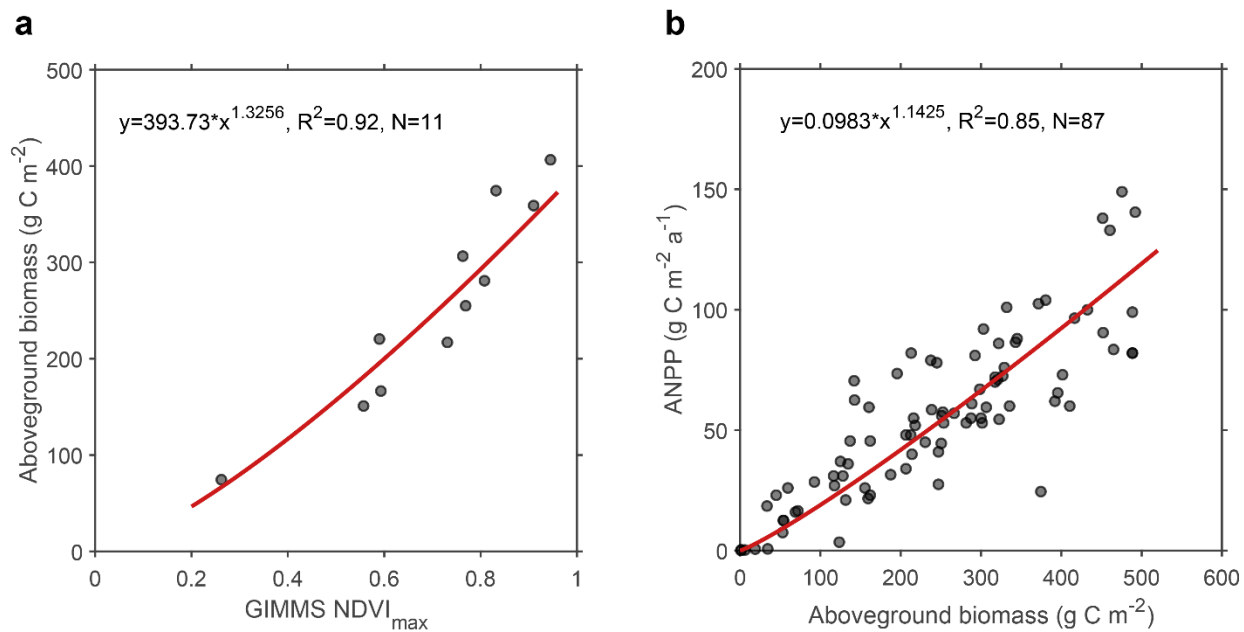


Figure S9. Spatial patterns of primary production in Tibetan Plateau (TP) grassland and Arctic tundra. a-b, gross primary production (GPP). c-d, net primary production (NPP). e-f, aboveground NPP (ANPP). g-h, belowground NPP (BNPP). i-j, BNPP in the 0-10cm layer. k-l, BNPP deeper than 10cm. Here, GPP datasets are from Jung et al. (2011) for Arctic tundra, and from Yao et al. (2017) for TP grassland.

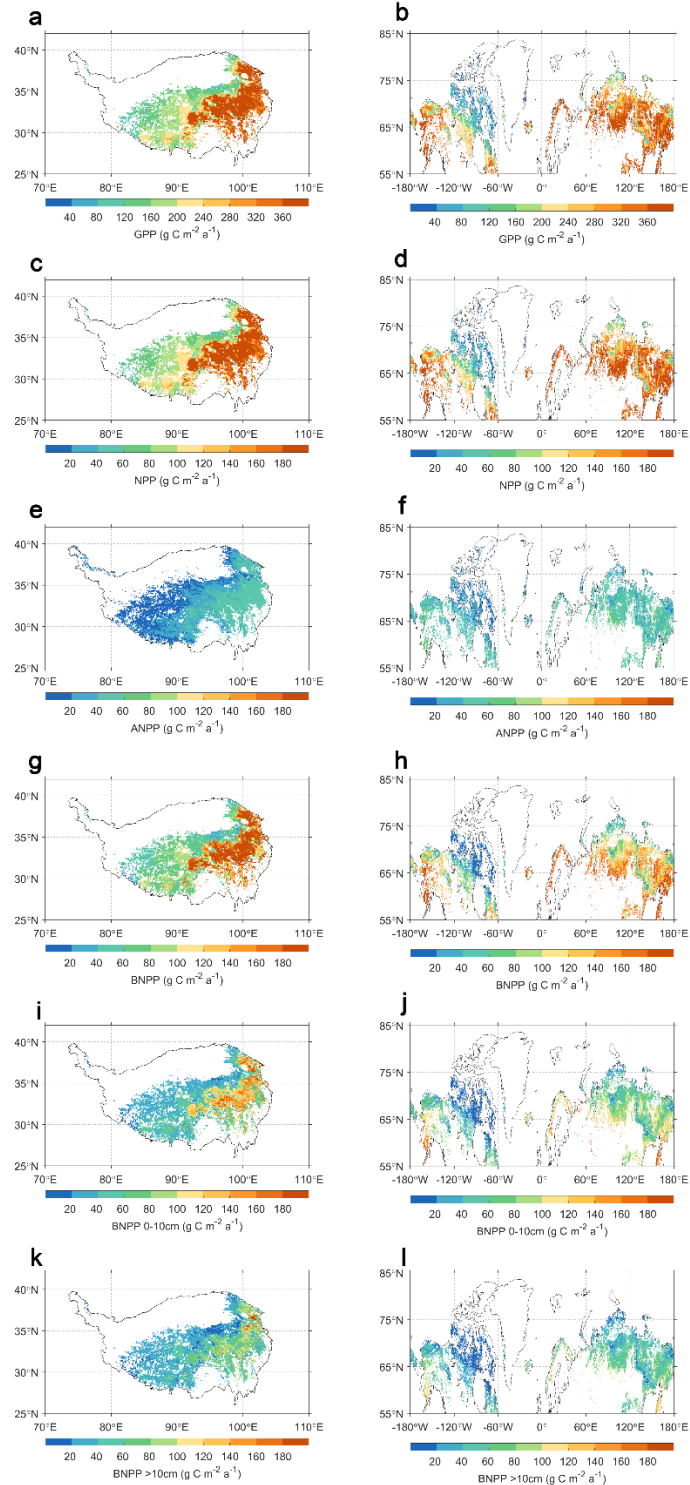


Figure S10. Histograms of primary production in Tibetan Plateau (TP) grassland and Arctic tundra. a, gross primary production (GPP). b, net primary production (NPP). c, aboveground NPP (ANPP). d, belowground NPP (BNPP). e, BNPP in the 0-10cm layer. f, BNPP deeper than 10cm. Values in parentheses are regional-mean primary productivity that is calculated by averaging gridded values over TP grassland and Arctic tundra, respectively. Here, GPP datasets are from Jung et al. (2011) for Arctic tundra, and from Yao et al. (2017) for TP grassland.

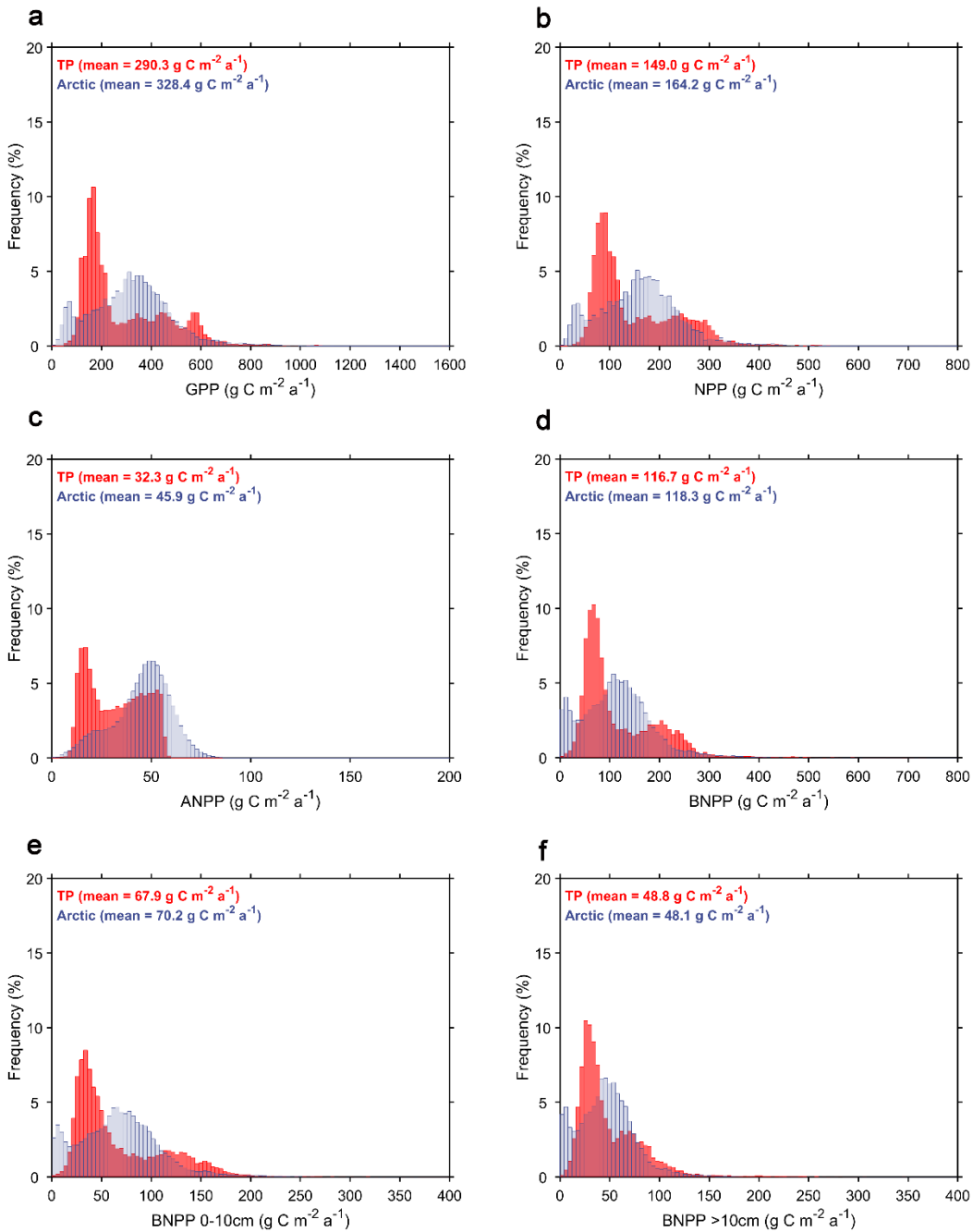


Figure S11. Spatial patterns of mean annual temperature (MAT), mean annual precipitation (MAP) and altitude in Tibetan Plateau (TP) grassland and Arctic tundra. a-b, MAT. c-d, MAP. e-f, altitude. MAT and MAP are derived from WorldClim Version 2.0 dataset; and altitude (elevation above sea level, m) is from the WorldClim Version 1.4 dataset.

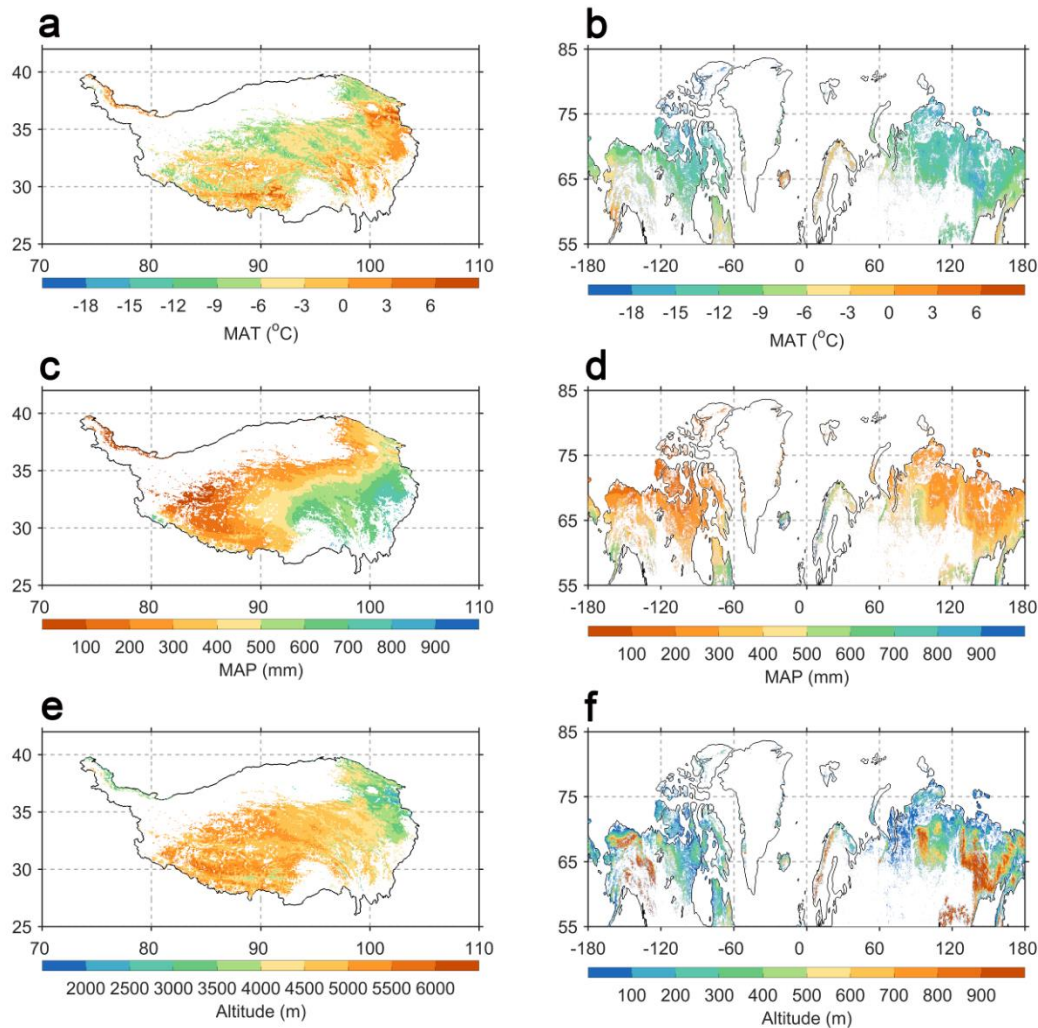


Figure S12. Histograms of mean annual temperature (MAT) and mean annual precipitation (MAP) using WorldClim Version 2.0 dataset in Tibetan Plateau (TP) grassland and Arctic tundra, respectively. a, MAT. b, MAP. MAT and MAP are derived from WorldClim Version 2.0 dataset. Values in parentheses are regional-mean climate that is calculated by averaging gridded values over TP grassland and Arctic tundra, respectively.

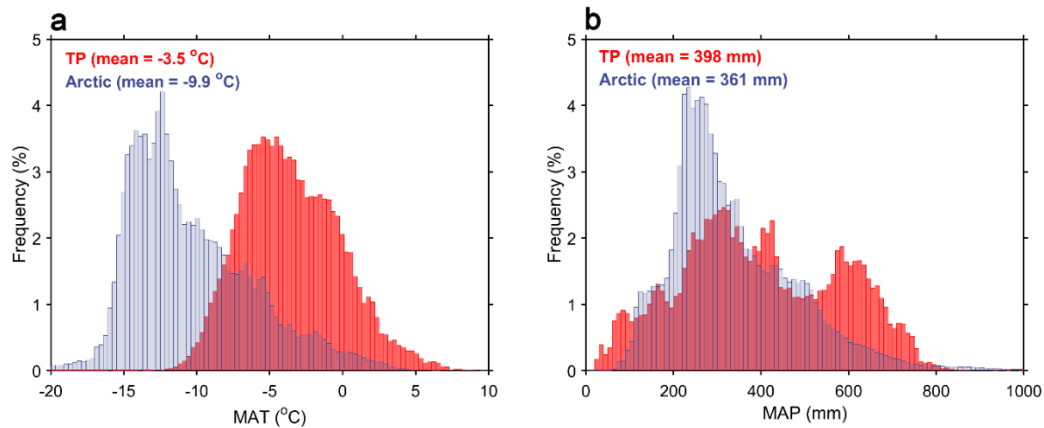


Figure S13. Histograms of mean annual solar radiation (MAR) and mean annual ultraviolet-B radiation (MUV-BR) in Tibetan Plateau (TP) grassland and Arctic tundra. a, MAR. b, MUV-BR. Solar radiation and ultraviolet-B radiation are used for indicating the potential degree of photodegradation in the two regions. MAR and MUV-BR are derived from WorldClim Version 2.0 and a global UV-B radiation dataset, respectively. Values in parentheses are regional-mean radiation that is calculated by averaging gridded values over TP grassland and Arctic tundra, respectively.

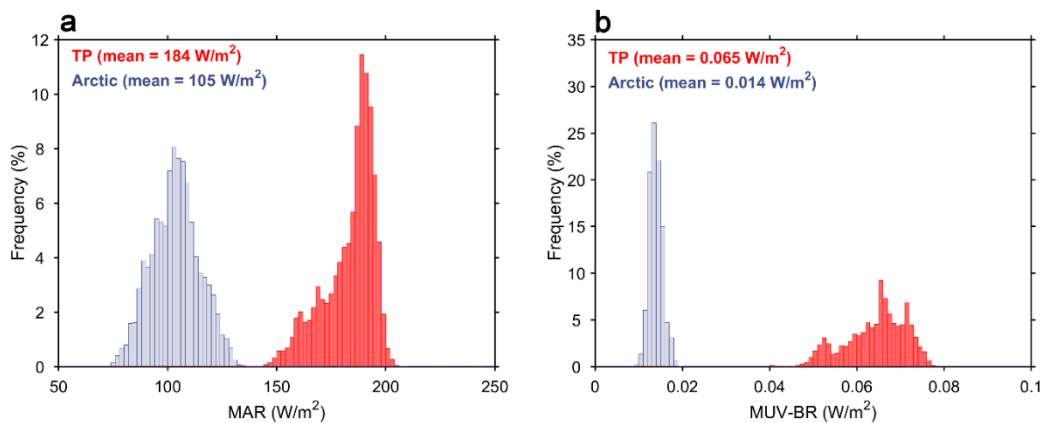


Figure S14. Histograms of physical soil properties from Soilgrid250m datasets in Tibetan Plateau (TP) grassland and Arctic tundra. a, clay content mass fraction (%). b, silt content mass fraction (%). c, sand content mass fraction (%). The soil property is derived from the SoilGrids dataset. Values in parentheses are regional-mean soil property that is calculated by averaging gridded values over TP grassland and Arctic tundra, respectively. Soil texture was derived based on a depth of 5 cm.

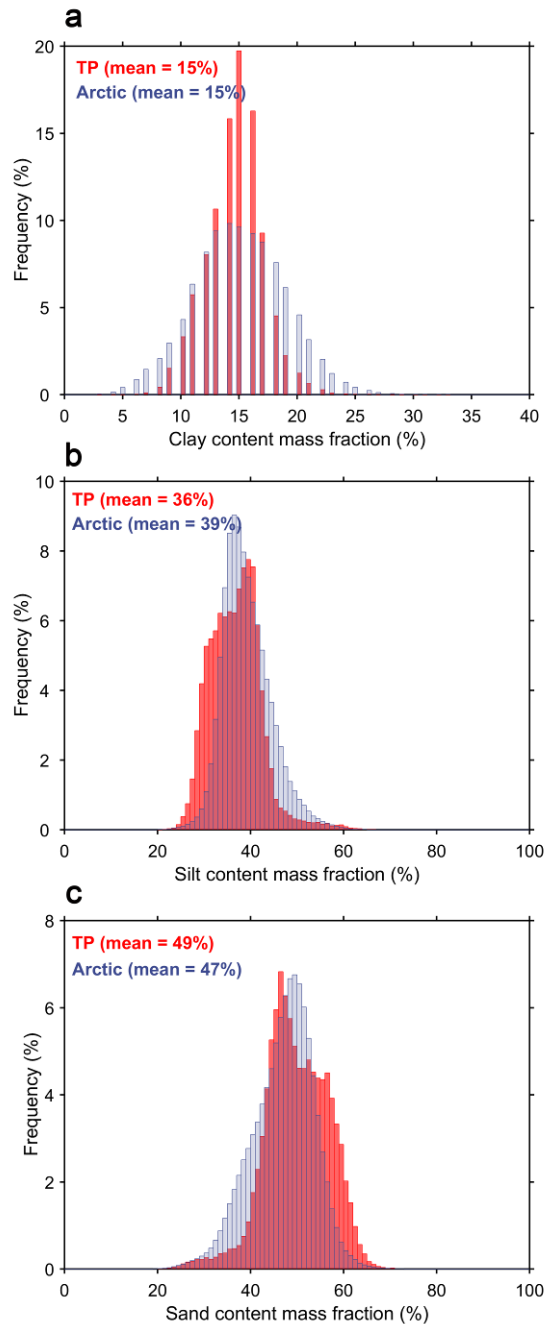


Figure. S15 Spatial patterns of primary production in Tibetan Plateau (TP) grassland and Arctic tundra. a-b, gross primary production (GPP). c-d, net primary production (NPP). e-f, aboveground NPP (ANPP). g-h, belowground NPP (BNPP). i-j, BNPP in the 0-10cm layer. k-l, BNPP deeper than 10cm. Here, GPP and NPP are from Bloom et al. (2016) for TP grassland and Arctic tundra.

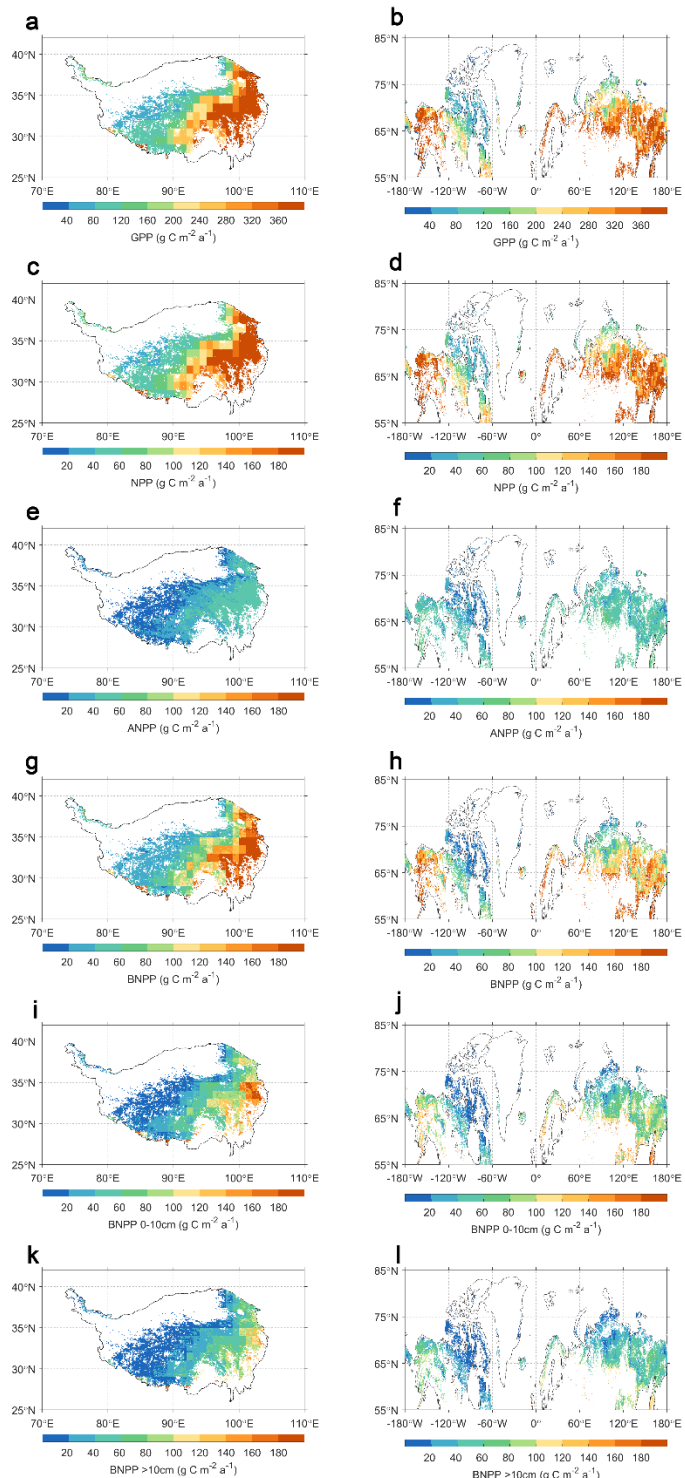


Figure S16. Histograms of primary production in Tibetan Plateau (TP) grassland and Arctic tundra. a, gross primary production (GPP). b, net primary production (NPP). c, aboveground NPP (ANPP). d, belowground NPP (BNPP). e, BNPP in the 0-10cm layer. f, BNPP deeper than 10cm. Values in parentheses are regional-mean primary productivity that is calculated by averaging gridded values over TP grassland and Arctic tundra, respectively. Here, GPP and NPP are from Bloom et al. (2016) for TP grassland and Arctic tundra.

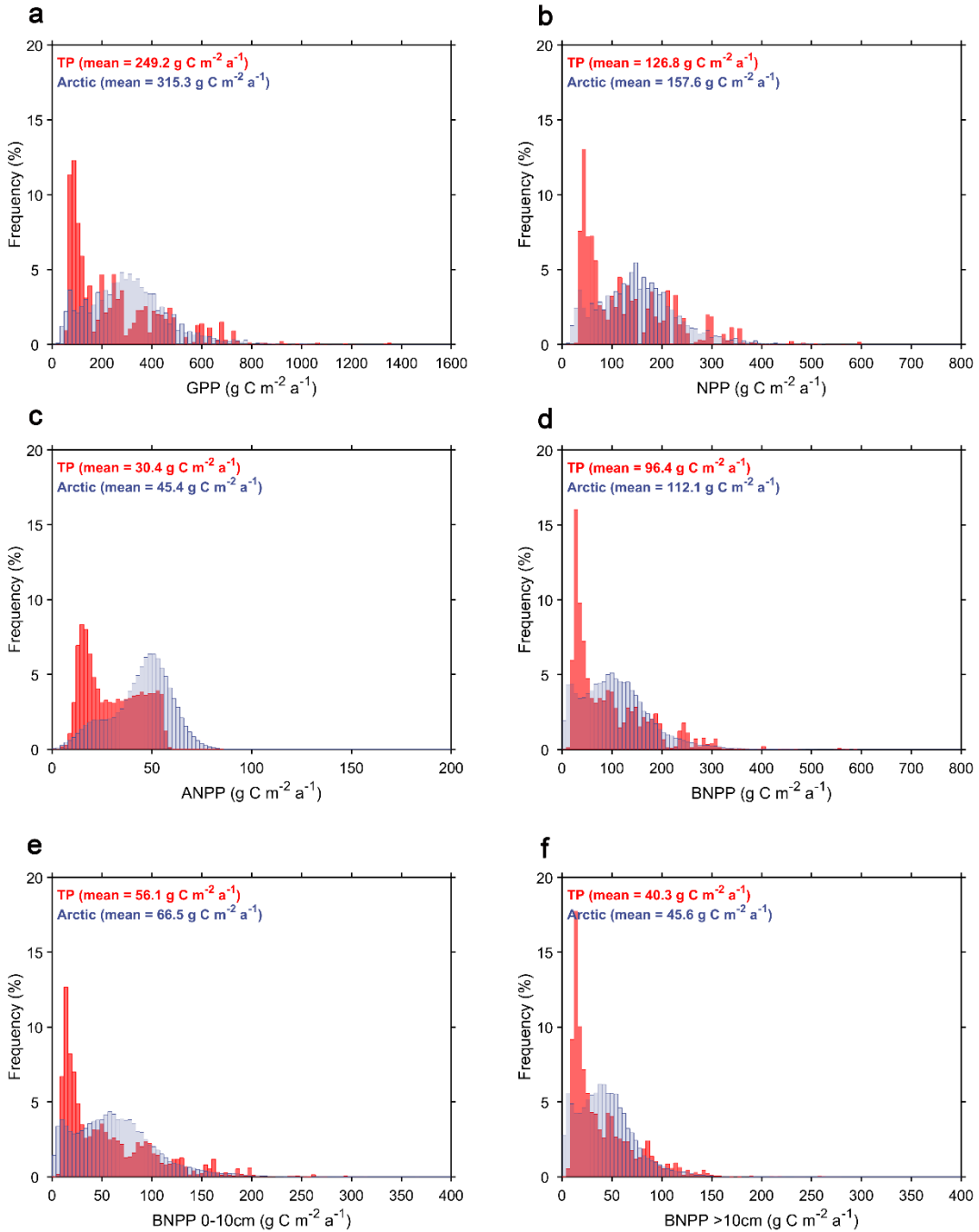


Figure S17. Spatial pattern of site-based SOC turnover time in topsoil (0-10cm). Pentagrams represent the SOC sites in Tibetan Plateau (TP) grassland (number = 21); triangles represent the SOC sites in arctic tundra (number = 10); and filled circles show SOC sites in other regions around the world (from He et al. (2016), number = 106).

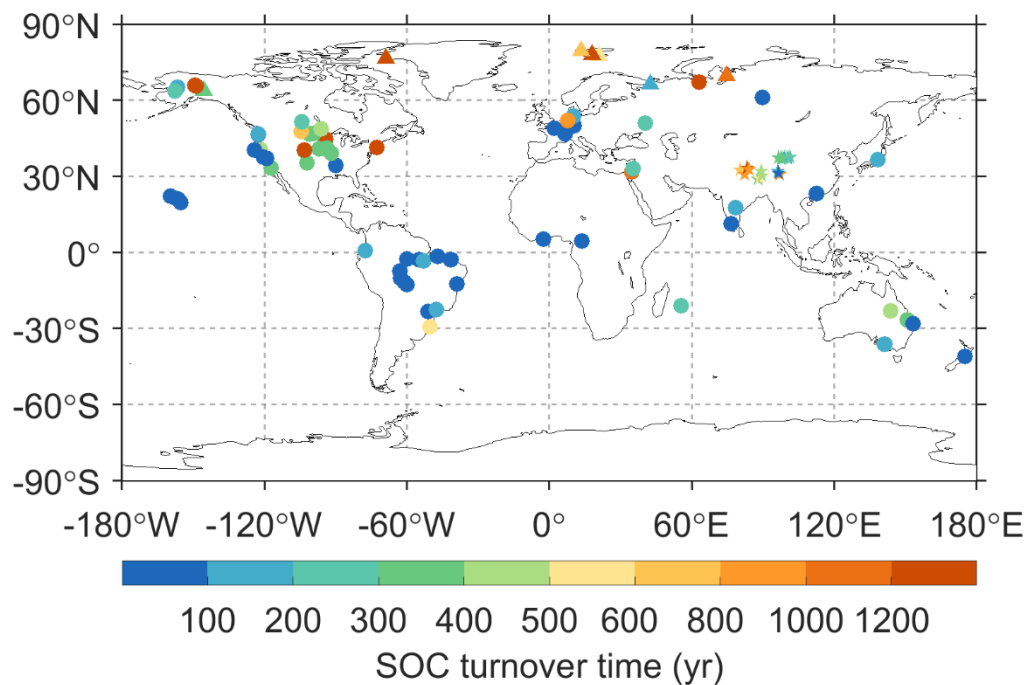


Figure S18. Distribution of SOC turnover time in topsoil (0-10cm) in the mean annual temperature (MAT) and mean annual precipitation (MAP) domain. Pentagrams represent the SOC sites in Tibetan Plateau (TP) grassland (number = 21); triangles represent the SOC sites in arctic tundra (number = 10); and filled circles show SOC sites in other regions around the world (from He et al. (2016), number = 106).

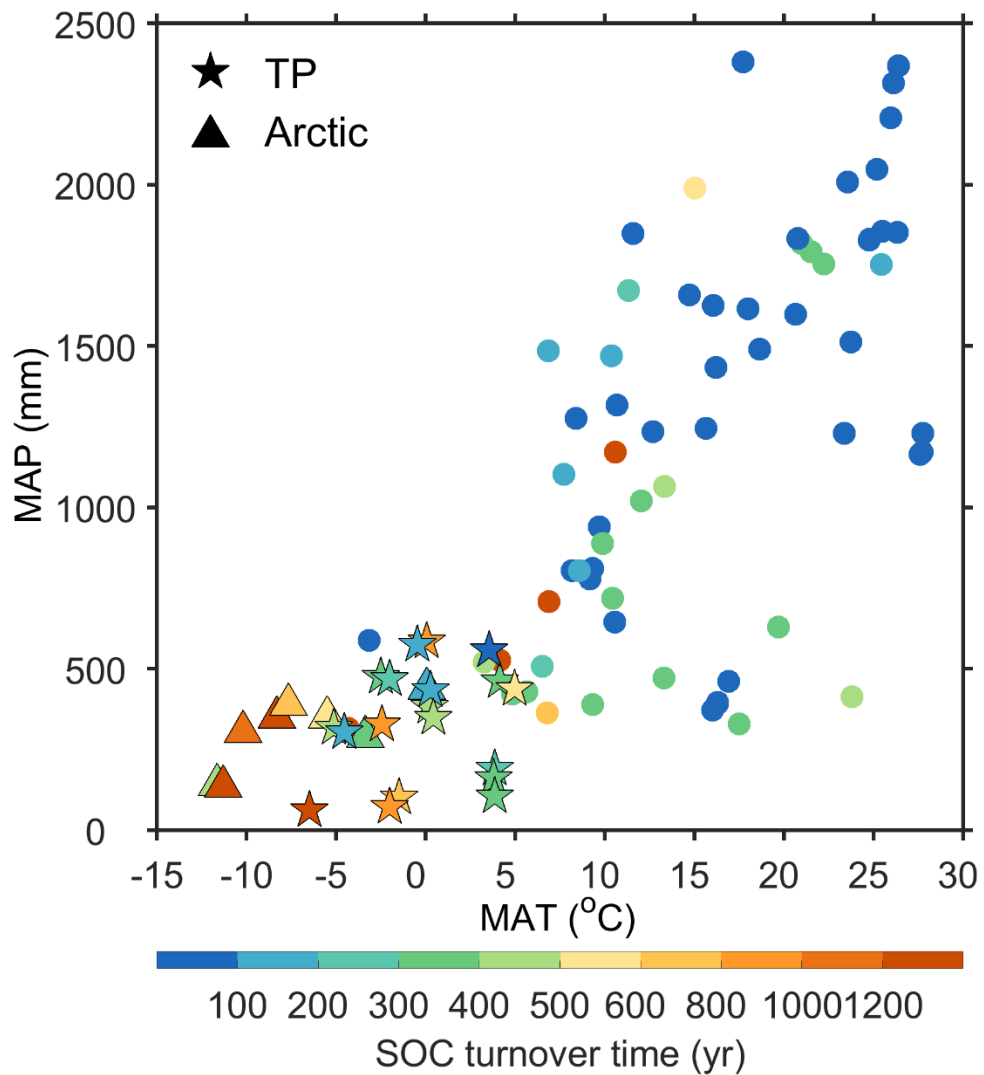


Figure S19. Relationships between topsoil organic carbon (SOC) turnover time and altitude. Here, carbon turnover times for all sites were converted from observed ^{14}C data using box model for a supposedly homogeneous reservoir.

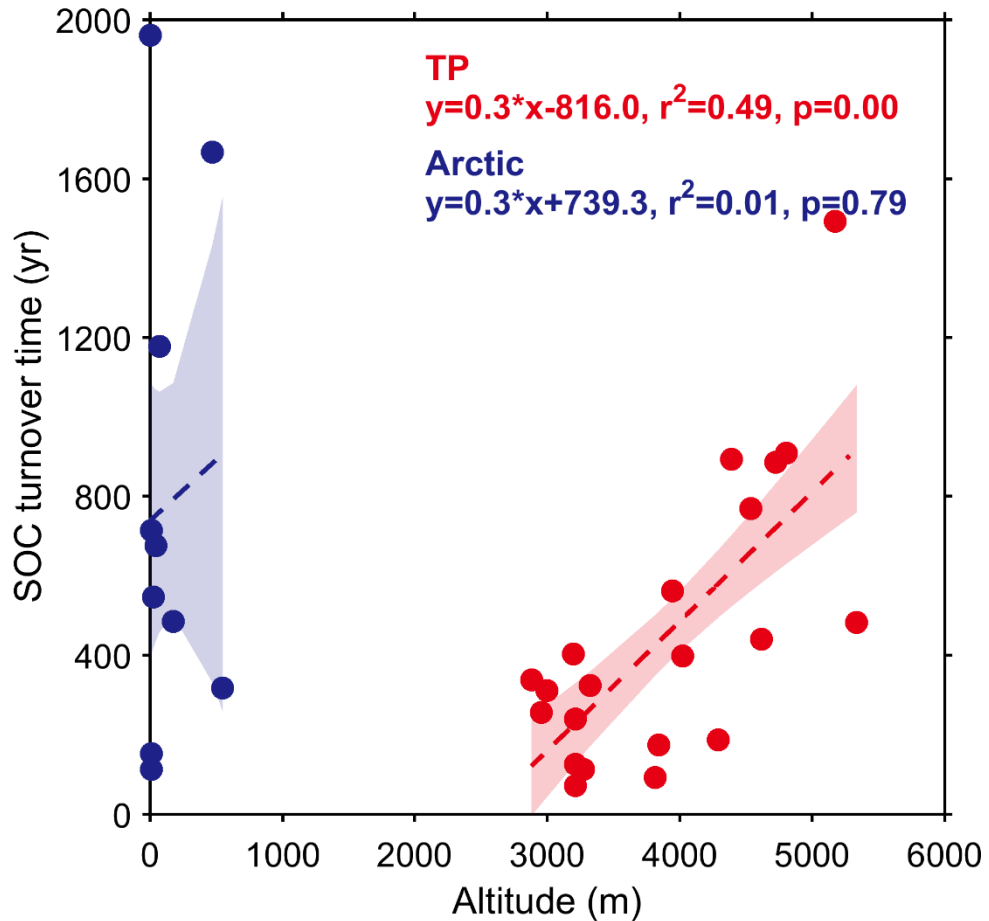


Figure S20. Spatial patterns of topsoil organic carbon (SOC) turnover times in Tibetan Plateau (TP) grassland and Arctic tundra. a, Tibetan Plateau grassland. b, Arctic tundra. Grey triangles in subfigures represent the locations of soil radiocarbon (^{14}C) measurement sites used in this study (21 locations in the TP grassland, and 10 locations in the Arctic tundra). The gridded turnover times (in years) in TP grassland and Arctic tundra are extrapolated from their own relationships between soil organic turnover times (SOC times) and environmental variables.

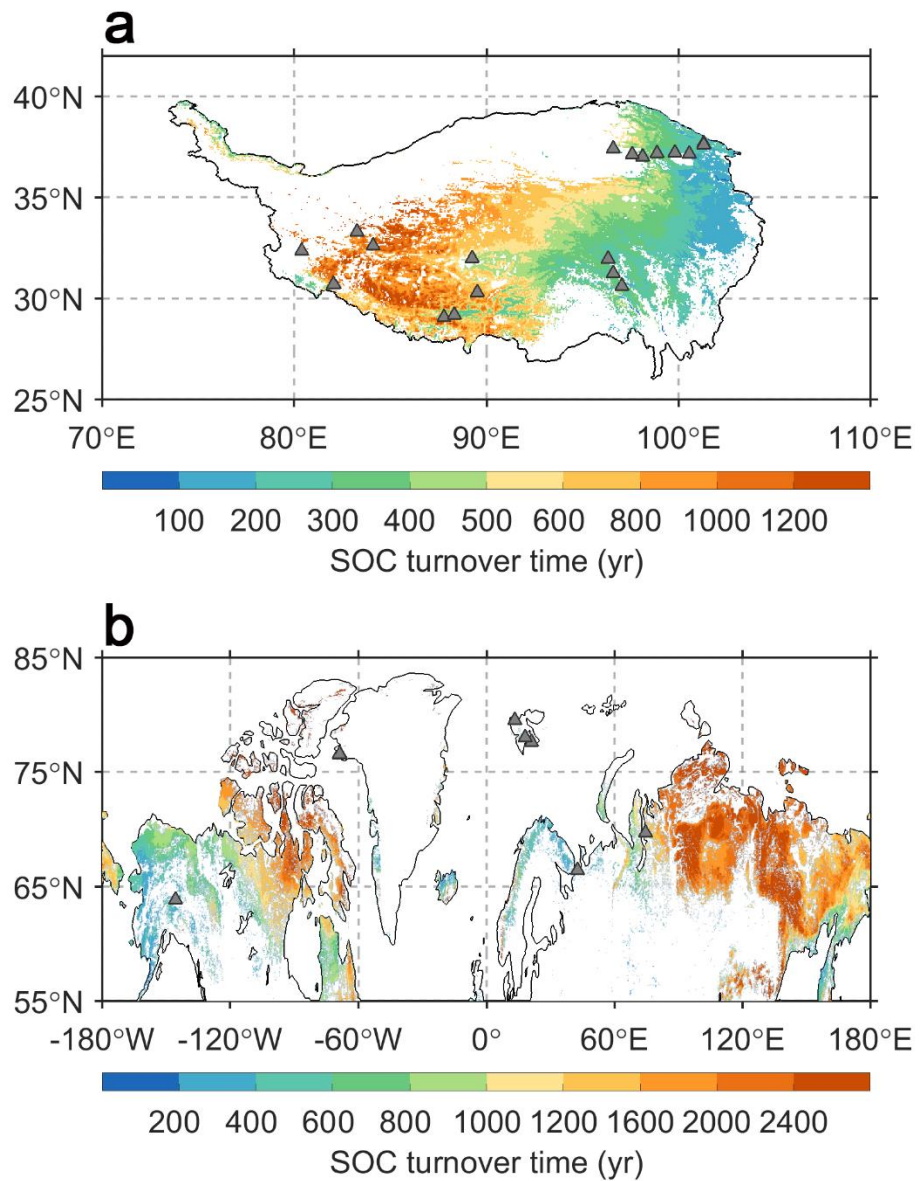


Figure S21. Uncertainties of spatial patterns of topsoil organic carbon (SOC) turnover time with 10th and 90th percentiles in Tibetan Plateau (TP) grassland and Arctic tundra. a-b, 10th percentile. c-d, 90th percentile. Here, 21 multiple linear regressions for TP grassland ($\ln(\text{SOC-turnover time}) \sim \text{latitude} + \text{MAP}$) and 10 relationships for Arctic tundra ($\ln(\text{(SOC-turnover time)}) \sim \text{MAT} + \text{MAP}$) were established by taking off one sample each time. The gridded turnover times (in years) in TP grassland and Arctic tundra are then extrapolated from these relationships; and 10th and 90th percentiles of the extrapolated maps are used to represent the uncertainty range of SOC turnover time in TP grassland and Arctic tundra.

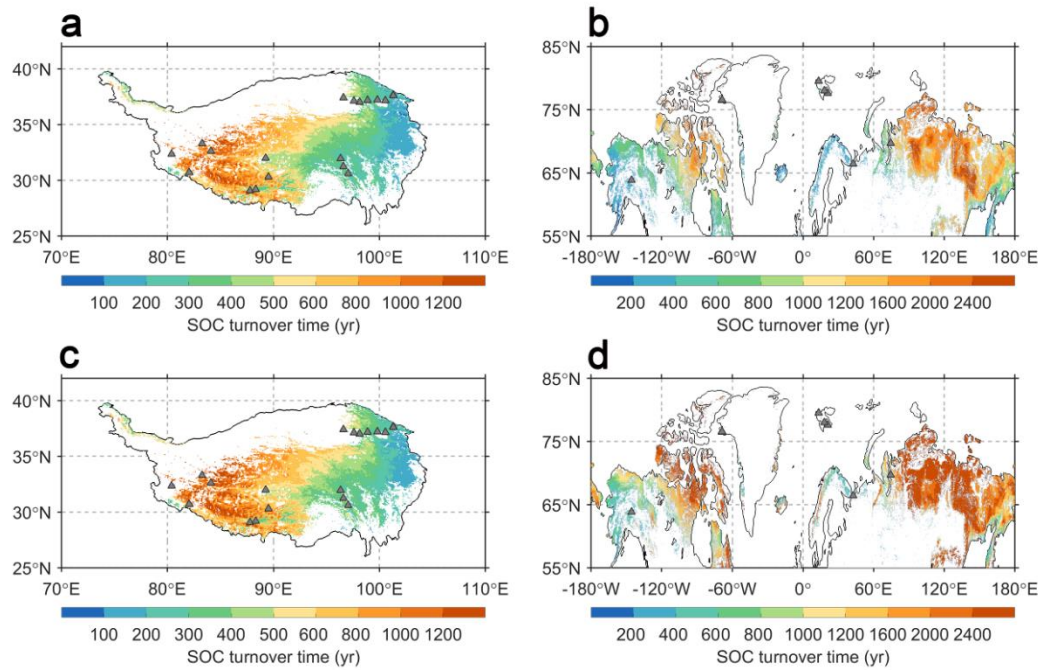


Figure S22. Uncertainties of topsoil organic carbon (SOC) turnover time with 10th and 90th percentiles in Tibetan Plateau (TP) grassland and Arctic tundra. a, 10th percentile. b, 90th percentile. See Supplementary Fig. 21 for details of the uncertainty analysis. Values in parentheses are regional-mean carbon turnover times that are calculated by averaging gridded values over TP grassland and Arctic tundra, respectively.

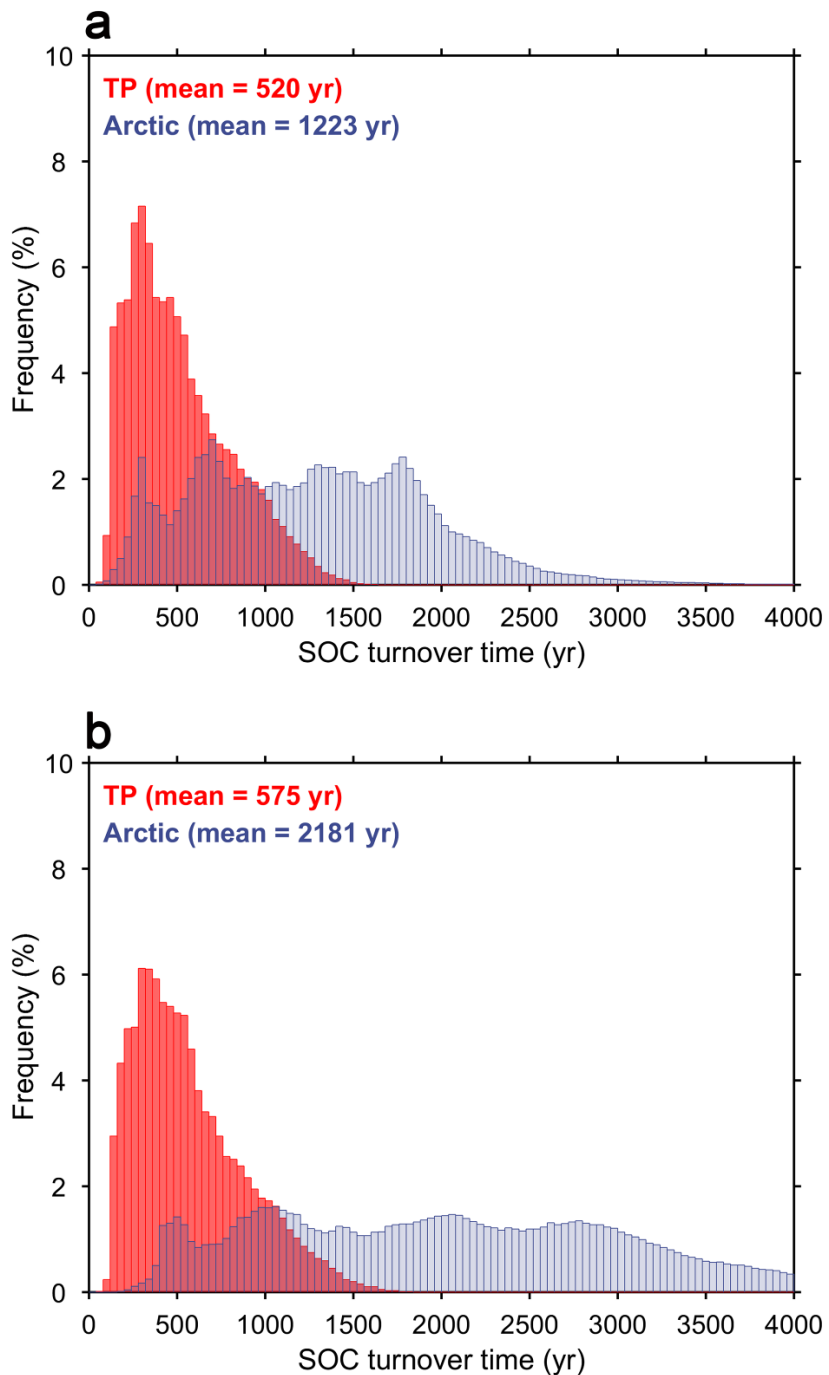


Figure S23. Uncertainties of topsoil organic carbon turnover time difference between TP grassland and Arctic tundra with 10th and 90th percentiles in the climate space. See Supplementary Fig. 21 for details of the uncertainty analysis. a, 10th percentile. b, 90th percentile. Difference of turnover times (Δ SOC turnover time, in years) is shown in each 1°C interval of mean annual temperature (MAT) and 25-mm interval of mean annual precipitation (MAP) climate space. The MAP and MAP which are calculated by averaging the period from 1970 to 2000 are derived from WorldClim Version 2.0 dataset. The SOC turnover times in TP grassland were shorter than those in Arctic tundra for 62% (10th percentile) and 76% (90th percentile) of the climate space.

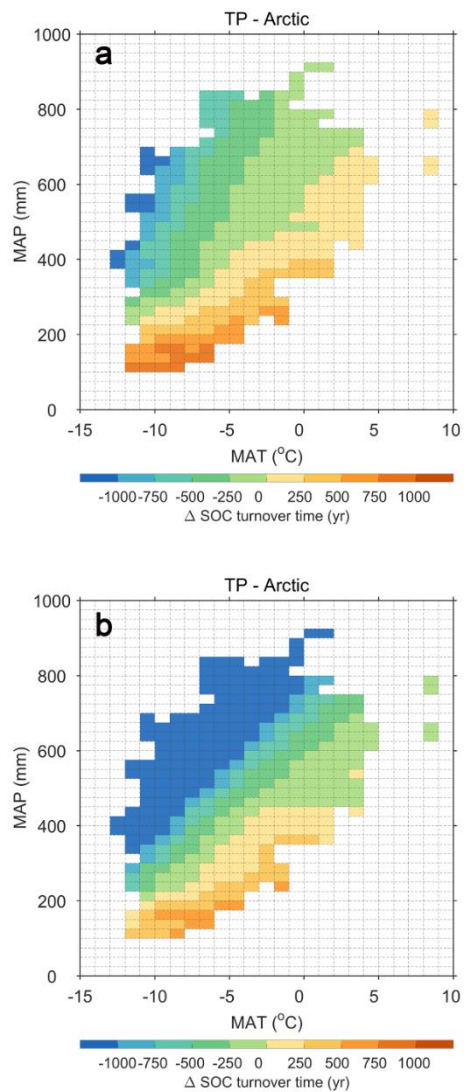


Figure S24. Ratio of carbon and nitrogen (C:N) in soil and microbes for TP grassland and Arctic tundra based on previous field investigations and meta-analyses (Chen et al. (2016) and Xu et al. (2013)).

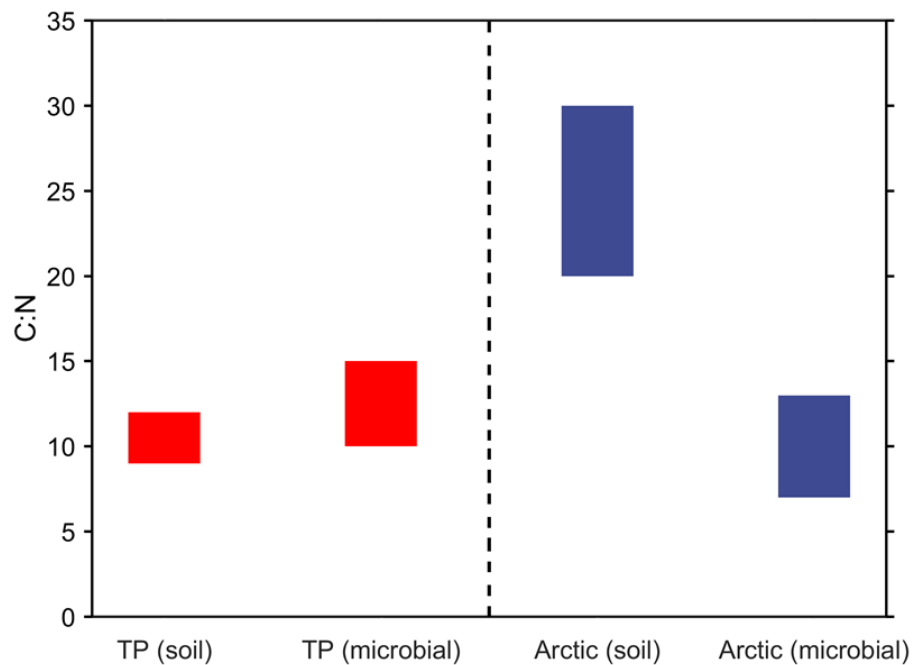


Figure 25. Percentages of human appropriation of NPP in TP grassland and Arctic tundra. a-b, spatial patterns of percentages of human appropriation of NPP (NPP_h of NPP). c, histograms of human appropriation of NPP (NPP_h). Here, mean represents area weighted value for each region. Values in parentheses are regional-mean NPP_h that is calculated by averaging gridded value over TP grassland and Arctic tundra, respectively. NPP_h of NPP is calculated as $(NPP_{act} - NPP_t)/NPP_{act}$ given by Haberl et al. (2007).

